RAA 2019 Vol. **19** No. **12**, 183(13pp) doi: 10.1088/1674–4527/19/12/183

http://www.raa-journal.org *http://iopscience.iop.org/raa*

Research in Astronomy and Astrophysics

Probing star formation and feedback using CCOSMA and archival data in the CFG028.68–0.28 quasi-sinusoidal filament

Jin-Long Xu[1,8,9], Jürgen Stutzki[2], Yuefang Wu[3], Xin Guan[1,8,9], Jun-Jie Wang[1,8,9], M. Miller[2], Yang Chen[4], Sheng-Li Qin[5], Jun-Zhi Wang[6], Chang-Chun Ning[7,9], Danzengluobu[7,9], Tian-Lu Chen[7,9], Nai-Ping Yu[1,8,9], Chuan-Peng Zhang[1,9], Xiao-Lan Liu[1,9], Jian-Bin Li[1,8,9], Karl Jacobs[2], Urs U. Graf[2], Gang Xu[1,8,9], Nan Li[1,9], Guo-Yin Zhang[1,9] and Qi Wu[7,9]

[1] National Astronomical Observatories, Chinese Academy of Sciences, Beijing 100101, China; *xujl@bao.ac.cn*
[2] I. Physikalisches Institut, Universität zu Köln, Zülpicher Str. 77, 50937 Köln, Germany
[3] Department of Astronomy, Peking University, Beijing 100871, China
[4] School of Astronomy and Space Science, Nanjing University, Nanjing 210023, China
[5] Department of Astronomy, Yunnan University, and Key Laboratory of Astroparticle Physics of Yunnan Province, Kunming 650091, China
[6] Shanghai Astronomical Observatory, Chinese Academy of Sciences, Shanghai 200030, China
[7] Tibet University, Lhasa, Tibet 850000, China
[8] CAS Key Laboratory of FAST, National Astronomical Observatories, Chinese Academy of Sciences, Beijing 100101, China
[9] NAOC-TU Joint Center for Astrophysics, Lhasa 850000, China

Received 2019 March 3; accepted 2019 July 22

Abstract We have performed a multi-wavelength study toward a quasi-sinusoidal filament (CFG028.68–0.28). A new large-scale ^{12}CO $J = 3-2$ map was obtained from the China-Cologne Observation for SubMillimeter Astronomy (CCOSMA) 3m radio telescope. Based on the ATLASGAL catalog, we have identified 27 dust clumps in the filament. Through the relationship between the mass and radius of these clumps, 67% of these clumps are dense and massive enough to potentially form massive stars. The obtained CFE is ∼11% in the filament. The filament has a linear mass density of ∼305 $M_\odot \mathrm{pc}^{-1}$, which is smaller than its critical mass to length ratio. This suggests that the external pressure from the neighboring H II regions may help prevent the filament from dispersing under the effects of turbulence. Comparing the energy injection from outflows and H II regions in the filament, the ionization feedback from the H II regions can help maintain the observed turbulence.

Key words: stars: formation —stars: early-type — ISM: H II regions — ISM: individual (CFG028.68-0.28, IRDC G28.53-0.25, and N49)

1 INTRODUCTION

The importance of interstellar filament for star formation is emphasized for the first time by Schneider & Elmegreen (1979). Since a wealth of filamentary structures in molecular clouds (MCs) have been revealed by dust continuum Galactic Plane surveys (Skrutskie et al. 2006; Molinari et al. 2010), the study of filaments has attracted much attention. Filamentary structures have wide ranges of masses (∼1-10^5 $M_\odot$) and lengths ($\sim 0.1 - 100$ pc), and typical temperatures in the range of $\sim 10 - 15$ K (e.g., Jackson et al. 2010; Seifried & Walch 2015; Beuther et al. 2015; Li et al. 2016; Wang et al. 2016; Kainulainen et al. 2017). The filaments are often associated with infrared dark clouds (IRDCs). The IRDCs are seen as dark absorption features against the Galactic background at mid-infrared wavelengths (e.g., Hennebelle et al. 2001; Simon et al. 2006; Peretto & Fuller 2009). The 8 μm emission shows infrared dark and bright parts, suggesting that each part of the IRDCs are at different evolutionary stages (Tackenberg et al. 2013; Xu et al. 2016; Veena et al. 2018). The bright parts of the IRDCs are often coincident with H II regions and infrared bubbles. The associated H II regions may illuminate the dark parts of the filament and make them bright, as described by Jackson et al. (2010). H II regions may play an important role in promoting the evolution of filamentary IRDC, thus more observations are needed to check this issue.

In addition, the filamentary IRDCs are considered as the precursors of massive stars and star clusters (Egan et al. 1998; Carey et al. 2000; Rathborne et al. 2006). Clumps and cores are often distributed along the filamentary IRDCs (André et al. 2010; Beuther et al. 2013; Contreras et al. 2016). However, the processes of filament fragmenting to star-forming cores and clumps are not well understood. The formation of cores and clumps can be regulated by the interplay between gravity, turbulence, and magnetic field (Li et al. 2015). The filaments may inherit their initial turbulence from the interstellar medium, but these motions have been shown to dissipate quickly (Stone et al. 1998; Mac Low 1999). Several ideas have been proposed to explain observed cloud energies, suggesting that cloud lifetimes may be short compared with the decay time (Elmegreen 2000). Gravitational collapse may drive turbulence (Robertson & Goldreich 2012), while energy injected by forming massive stars may sustain turbulence (Krumholz et al. 2014). On parsec scales, both observation and numerical simulation indicate that the energies associated with protostellar outflows, winds, and radiations are comparable to the cloud turbulence energy (Offner & Liu 2018).

A quasi-sinusoidal filament (CFG028.68–0.28) was first identified from the *Herschel* Infrared Galactic Plane survey by Wang et al. (2015). The CFG028.68–0.28 filament is also associated with IRDC G28.53–0.25. IRDC G28.53–0.25 is at a kinematic distance of 5.4 kpc (Rathborne et al. 2006) with a luminosity of $\sim 3500L_{\odot}$ (Rathborne et al. 2010). In the 1.2 mm continuum emission, IRDC G28.53–0.25 shows a filamentary structure that extends about $5'$ with a mass of $\sim 10^4 M_{\odot}$ (Rathborne et al. 2006). Several cores and clumps are detected in high angular resolution observations in G28.53-0.25 (Rathborne et al. 2006, 2010; Sanhueza et al. 2012; Lu et al. 2015). Lu et al. (2015) found that some cores are associated with outflows, masers, and infrared sources, suggesting that the star formation is taking place in IRDC G28.53–0.25. In this paper, we investigate the activities of star formation and feedback toward the CFG028.68-0.28 filament using multi-wavelength data. Our observations and data reduction are described in Section 2, and the results are presented in Section 3. In Section 4, we will discuss the structure and property of the filament, and clump formation in the filament, while our conclusions are summarized in Section 5.

2 OBSERVATION AND DATA PROCESSING

2.1 CCOSMA Data

We made the $40' \times 30'$ mapping observations toward the CFG028.68–0.28 filament in the transition of ^{12}CO $J = 3-2$ line (rest frequency is 345.789 GHz) using the China-Cologne Observation for SubMillimeter Astronomy (CCOSMA) 3m radio telescope at Yangbajain in Tibet in the west of China at an altitude of 4300 m, during January 2019. The predecessor of CCOSMA is the Kölner Observatorium für SubMillimeter Astronomie (KOSMA[1]). The half-power beam width of the telescope at observing frequency of 345 GHz is $83''$. The pointing and tracking accuracy is better than $10''$. The tuning frequency of the receiver ranges from 330 GHz to 365 GHz with a bandwidth of 1 GHz. In this frequency range, we can detect the notable lines, such as ^{12}CO $J = 3-2$, ^{13}CO $J = 3-2$, C^{18}O $J = 3-2$, and HCO$^+$ $J = 4-3$. In this paper, we only observed ^{12}CO $J = 3-2$ line for the CFG028.68–0.28 filament. The back end is a fast Fourier transform spectrometer (FFTS) of 32768 channels with a bandwidth of 2.5 GHz, corresponding to a velocity resolution of 0.077 km s^{-1}. The system noise temperature (Tsys) is 301 K in a single-sideband scale. The beam efficiency $B_{\rm eff}$ is 0.72 at 345 GHz, and the forward efficiency $F_{\rm eff}$ is 0.93. The mapping was done using on-the-fly (OTF) mode with a $1' \times 1'$ grid. Because the OTF map of the ^{12}CO $J = 3-2$ data is under Nyquist sampling, we smoothed the CCOSMA data ($92''$) to angular resolution of $120''$. Compared with the JCMT data, we also smoothed the CCOSMA data to a velocity resolution of 1 km s^{-1}. The correction for the line intensity to the main beam temperature scale was made using the formula $T_{\rm mb} = (F_{\rm eff}/B_{\rm eff} \times T_{\rm A}^*)$. The data were reduced using the GILDAS/CLASS[2] package.

2.2 Archival Data

In order to obtain a ^{13}CO $J = 1-0$ view of the CFG028.68–0.28 filament, we used the Galactic Ring Survey (GRS) data of ^{13}CO $J = 1-0$ emission using the Five College Ra-dio Astronomy Observatory (FCRAO) (Jackson et al. 2006). The survey covers a longitude range of ℓ=18.0°–55.7° and a latitude range of $|b|\leq 1°$, with an angular resolution of $46''$. At a velocity resolution of 0.21 km s^{-1}, the typical rms sensitivity is 0.13 K. Moreover, ^{12}CO $J = 3-2$ and ^{13}CO $J = 3-2$ data are obtained from the JCMT High-Resolution Survey (COHRS, Dempsey et al. 2013) and Heterodyne Inner Milky Way Plane Survey (CHIMPS, Rigby et al. 2016). The COHRS

[1] `https://astro.uni-koeln.de/17647.html`
[2] `http://www.iram.fr/IRAMFR/GILDAS`

has an angular resolution of 16.6″ and a velocity resolution of 1 km s^{-1}, while CHIMPS has an angular resolution of 15.2″ and velocity resolution of 0.5 km s^{-1}. In calculation and comparing images (Figs. 1 and 2), we smoothed the FCRAO and JCMT data to the same angular resolution with the CCOSMA data (120″).

To explore the dust distribution, we used far-infrared data (70 μm–500 μm) from the *Herschel* Infrared Galactic Plane survey (Hi-GAL; Molinari et al. 2010) carried out by the *Herschel* Space Observatory. The initial survey covered a Galactic longitude region of $300°<\ell<60°$ and $|b|<1.0°$. The Hi-GAL survey used two instruments: PACS (Poglitsch et al. 2010) and SPIRE (Griffin et al. 2010) in parallel mode to carry out a survey of the inner Galaxy in five bands: 70, 160, and 250 μm of PACS, 350 and 500 μm of SPIRE. The scan speeds of PACS is 20″ per second, while 30″ per second for SPIRE. The angular resolutions of these five bands are 10.7″, 11.4″, 18.2″, 24.9″, and 36.3″, respectively. The Hi-GAL data have been used to explore the flux density distribution and to construct column density map.

The GLIMPSE survey observed the Galactic plane ($65° < |l| < 10°$ for $|b| < 1°$) at the four IR bands (3.6, 4.5, 5.8, and 8.0 μm) of the Infrared Array Camera (IRAC) (Benjamin et al. 2003) on the *Spitzer* Space Telescope, we used the 8.0 μm data to identify H II regions. The angular resolution of the 8.0 μm band is 1.9″. We also use the MAGPIS survey (Multi-Array Galactic Plane Imaging Survey) to trace ionized gas of H II regions (Helfand et al. 2006). Data are collected in the B, C, and D configurations of the VLA operating in pseudocontinuum mode at 1.4 GHz. The MAGPIS survey has a beam size of 6″ and a typical rms of 0.3 mJy.

3 RESULTS

3.1 The Filament's CO and Radio Continuum Emission

Figure 1 shows the channel maps of the filament in ^{12}CO $J = 3-2$ from JCMT (blue contours) and CCOSMA (grey scale). It can be seen that the ^{12}CO $J = 3-2$ emission detected in the velocity range between 83.5 and 95.5 km s^{-1} displays a quasi-sinusoidal filamentary structure. To further compare the observed data from CCOSMA with that from JCMT, we extract spectra of ^{12}CO $J = 3-2$ from the same position, which is shown in Figure 2. Both the ^{12}CO $J = 3-2$ spectra show the approximately same profile. From the Figure 2, we see that the ^{12}CO $J = 3-2$ profiles show two peaks. Dewangan et al. (2017) confirmed that the two peaks indicate two component in ^{13}CO line. They further concluded that there exists cloud–cloud collision process in this region. Using the velocity range given above, we made a three-color CO integrated intensity map for the filament, as shown in Figure 3. The three CO emission shown are the CCOSMA ^{12}CO $J = 3-2$ (in red), FCRAO ^{13}CO $J = 1-0$ (in green), and JCMT ^{13}CO $J = 3-2$ (in blue). In Figure 3, the different CO emissions appear to highlight different layers of the filament. Compared with the ^{13} CO $J = 1-0$ emission, the ^{12}CO $J = 3-2$ emission may traces the relatively dense layer. Most obviously, the ^{13}CO $J = 3-2$ emission traces the densest layer (blue color) of the filament. The Hi-GAL survey data can be used to construct a column density map ($N_{\mathrm{H_2}}$) of the hydrogen molecule. Based on the smoothed 250 μm method of Palmeirim et al. (2013), the column density map of the filament with an angular resolution of 18.″2 was created using a modified blackbody model to fit the SEDs pixel by pixel. In Hi-GAL five bands, we only use 160 μm, 250 μm, 350 μm and, 500 μm. Emission at 70 μm was excluded in the SED fitting because it can be contaminated by emission from small grains in hot PDRs. The dust opacity law is assumed as $\kappa_\upsilon = 0.1\times(300\,\mu m/\lambda)^\beta$ cm^2/g, with β=2 (Palmeirim et al. 2013). Figure 4 displays the $N_{\mathrm{H_2}}$ map overlaid with the ^{12}CO $J = 3-2$ and ^{13}CO $J = 1-0$ emission. From Figure 4, we see that the $N_{\mathrm{H_2}}$ map (grey scale) shows four dense regions, which are well associated with the ^{12}CO $J = 3-2$ and ^{13}CO $J = 1-0$ emission. Two of the dense regions are consistent with two small scale of 870 μm dust filaments (G28.562–0.238 and G28.706–0.289) identified by Li et al. (2016), which are marked by two red dashed lines in upper panel of Figure 4. Adopting a distance of 5.4 kpc (Rathborne et al. 2006), the CFG028.68–0.28 filament extends about 63 pc (40′) in length, while the mean width is about 12 pc (8′), as traced by the ^{13}CO $J = 1-0$ emission.

3.2 The Filament's Column Density and Mass

Compared with the CO data, the column density map derived from Hi-GAL survey data does not show a completed filamentary structure. We use the ^{13}CO $J = 1-0$ emission to determine the column density and mass of the CFG028.68–0.28 filament. Assuming local thermodynamic equilibrium (LTE), the column density was estimated via Garden et al. (1991)

$$N(^{13}\mathrm{CO}) = 4.71\times10^{13}\frac{T_{\mathrm{ex}}+0.88}{\exp(-5.29/T_{\mathrm{ex}})} \times \frac{\tau(^{13}\mathrm{CO})}{1-\exp(-\tau(^{13}\mathrm{CO}))}\int T_{\mathrm{mb}}dv\ \mathrm{cm}^{-2}, \quad (1)$$

where τ is the optical depth, dv is the velocity range, and T_{mb} is the corrected main-beam temperature of ^{13}CO $J = 1-0$. T_{ex} is the mean excitation temperature of the molecular gas. Generally, the ^{12}CO emission is optically thick, so we used ^{12}CO $J = 3-2$ to estimate T_{ex} via

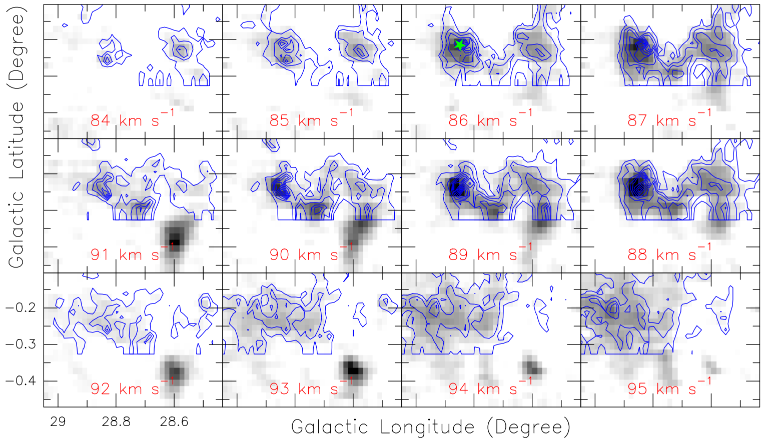

Fig. 1 The JCMT ^{12}CO $J = 3-2$ channel maps (*blue contours*) superimposed on that (*grey scale*) from the CCOSMA ^{12}CO $J = 3-2$. The integrated emission is in step of 1 km s^{-1}. Central velocities are indicated in each subimage. The green star marks the extracted position of ^{12}CO $J = 3-2$ line.

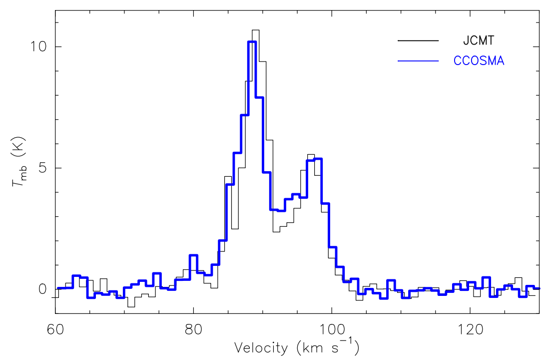

Fig. 2 Extracted spectra of ^{12}CO $J = 3-2$ from JCMT (*clack line*) and CCOSMA (*blue line*) data. The extracted position is marked by green star in Fig. 1.

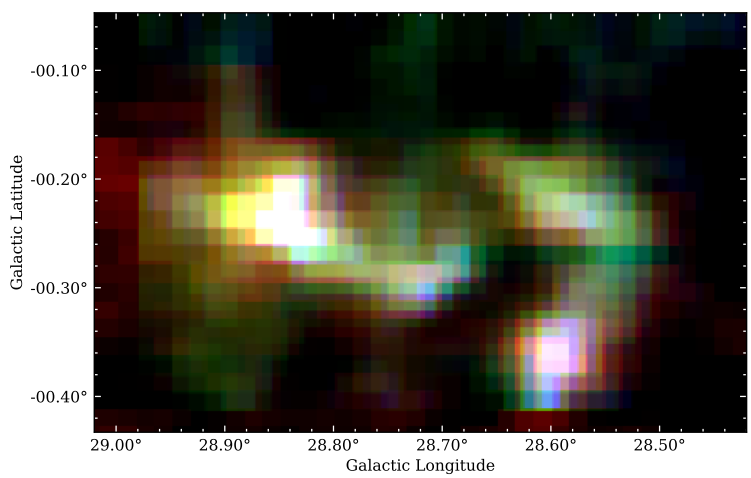

Fig. 3 Three-colour composite integrated intensity image of the filament using CCOSMA ^{12}CO $J = 3-2$ (*red*), FCRAO ^{13}CO $J = 1-0$ (*green*), and JCMT ^{13}CO $J = 3-2$ (*blue*).

following the equation (Garden et al. 1991)

$$T_{\rm ex} = \frac{16.6}{\ln[1 + 16.6/(T_{\rm mb} + 0.04)]}, \qquad (2)$$

Using all emissions greater than 5σ, we calculate the excitation temperature of each observed point. Since there are two velocity components along the line of sight toward the filament, we used two-velocity Gaussian components to fit each spectrum, and then obtain $T_{\rm mb}$ and linewidth. From Figure 5 (b panel), we find that the excitation temperature

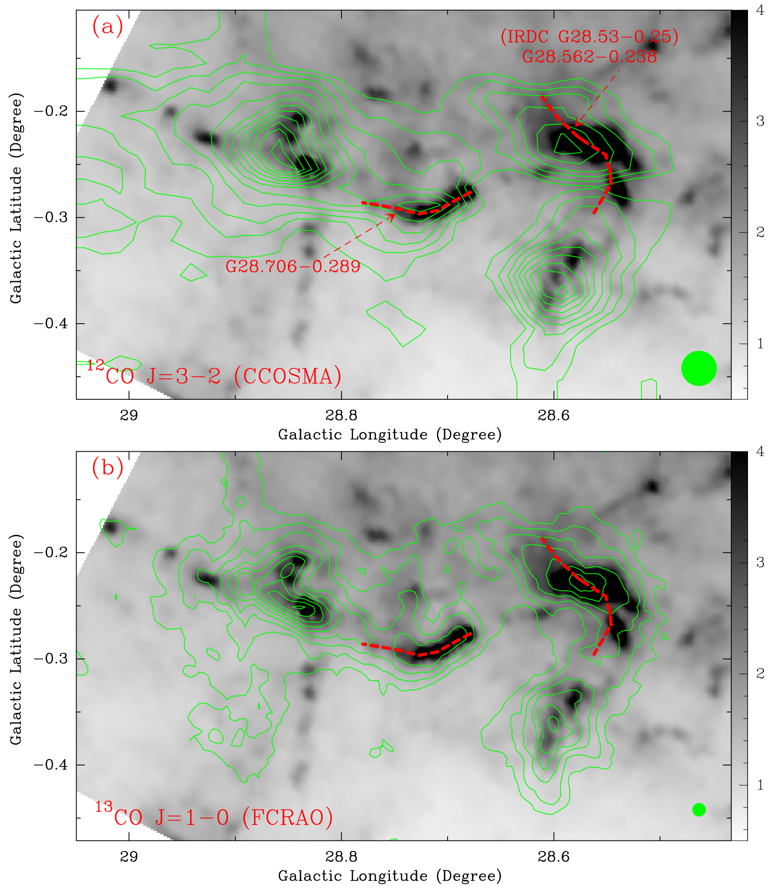

Fig. 4 (a) ^{12}CO $J = 3 - 2$ integrated intensity contours overlaid on column density map derived from Hi-GAL survey data. The green contour levels start from 3.6 (3σ) to 45.2 by a step of 3.5 K km $^{-1}$. (b) ^{13}CO $J = 1 - 0$ integrated intensity contours overlaid on column density map. The green contour levels are from 5.0 (3σ) to 25.0 by a step of 2.5 K km s^{-1}. The beams are shown as the green filled circles in the right corner. The right colour bar is in units of 10^{22} cm^{-2}.

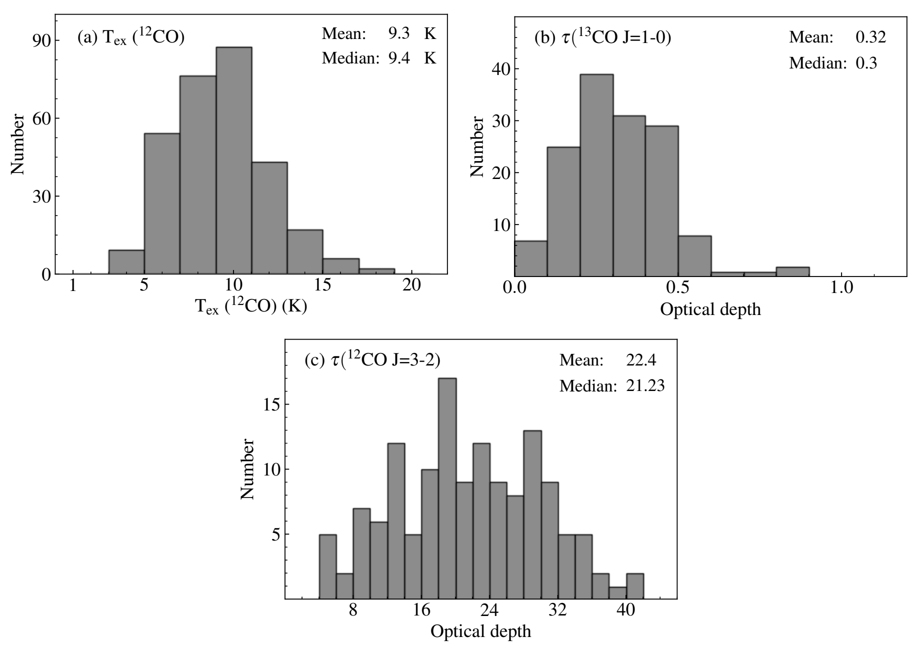

Fig. 5 Distribution of the excitation temperature and optical depth. The number is all observed point whose emission is greater than $5\,\sigma$.

is 4.4–18.0 K, while the mean excitation temperature of the filament is about 9.3 K.

In addition, we assumed that the excitation temperatures of ^{12}CO $J = 3-2$ and ^{13}CO $J = 1-0$ have the same value in the filament. τ can be obtained by the following equation (Garden et al. 1991)

$$\tau(^{13}\mathrm{CO}) = -\ln[1 - \frac{T_{\mathrm{mb}}}{5.29/[\exp(5.29/T_{\mathrm{ex}}) - 1] - 0.89}], \tag{3}$$

Using the equation above, the derived $\tau(^{13}\mathrm{CO})$ is 0.1–0.8, suggesting that the ^{13}CO $J = 1-0$ emission is optically thin in the filament. The abundance ratios of $[\mathrm{CO}]/[\mathrm{H_2}] = 10^4$ (Frerking et al. 1982a). Using the relation $N(\mathrm{H_2})/N(^{13}\mathrm{CO}) \approx 7 \times 10^5$ (Frerking et al. 1982b), we also obtained that the ^{12}CO $J = 3-2$ optical depth is 4.3–58.0, further confirming that the ^{12}CO $J = 3-2$ emission is optically thick in the filament. In Figure 5(b) and (c) panels show the optical depth distributions of the ^{13}CO $J = 1-0$ and ^{12}CO $J = 3-2$ emission.

Using the equation above, we obtained that the column density ranges between 1.0×10^{21} cm^{-2} and 1.2×10^{22} cm^{-2} with a mean column density of $(5.7\pm0.3)\times10^{21}$ cm^{-2}. In Figure 2, the ^{13}CO $J = 1-0$ emission is well associated with that of ^{12}CO $J = 3-2$. For comparison, we also estimate the mean column density of the filament in ^{12}CO $J = 3-2$ line by using the conversion factor $N(\mathrm{H_2})/\mathrm{W}(^{12}\mathrm{CO}\ J = 3-2) \simeq 4.0 \times 10^{20} \mathrm{cm^{-2} K^{-1} km^{-1} s}$ (Colombo et al. 2019), where W(^{12}CO $J = 3-2$) is the mean integrated intensity of ^{12}CO emission, which is 12.8 K km s^{-1} in the filament. By adopting the W(^{12}CO $J = 3-2$) value, we derive that the mean column density is about 5.1×10^{21} cm^{-2}, which is approximately equal to that derived by the ^{13}CO $J = 1-0$ emission. Generally, filaments display approximately long cylindrical structures (Jackson et al. 2010), thus the mass of the filament can be estimated by

$$M_{\mathrm{H_2}} = \pi(\frac{w}{2})^2 l \mu_g m(\mathrm{H_2}) n(\mathrm{H_2}), \tag{4}$$

where μ_g=1.36 is the mean atomic weight of the gas, while $m(\mathrm{H_2})$ is the mass of a hydrogen molecule. l and w are the length and mean width of the filament, respectively. The mean number density of $\mathrm{H_2}$ is given to be $n(\mathrm{H_2}) = 8.1 \times 10^{-20} N(\mathrm{H_2})/w$ (Garden et al. 1991). Using the mean width w (12 pc) of the filament, we derive the mean number density of 38.2 ± 2.2 cm^{-3} for the filament. By using the mean number density, we obtain a mass of $(1.9\pm0.1) \times 10^4 M_{\odot}$.

3.3 H II Regions/Infrared Bubbles Associated with the Filament

Figure 6(a) shows the ^{13}CO $J = 1-0$ emission map (blue contours) superimposed on the *Spitzer*-IRAC 8 μm emission map (grey scale) of CFG028.68–0.28. From the ^{13}CO $J = 1-0$ emission, we see that CFG028.68–0.28 shows a long filamentary structure. At 8 μm, CFG028.68–0.28 only displays a dark extinction feature at the middle section. At each end sections of the CFG028.68–0.28 filament, we find some bright *Spitzer*-IRAC 8 μm emission. The bright 8 μm emission is attributed to polycyclic aromatic hydrocarbons (PAHs) (Leger & Puget 1984), which can be used to delineate an infrared bubble. Infrared bubbles are highlighted by the bright 8.0 μm emission surrounding O and early-B stars (Churchwell et al. 2006). From the Churchwell et al. (2006) and Simpson et al. (2012) catalogues, we find seven infrared bubbles in the filament, whose parameters are listed in Table 2. In order to facilitate the discussion and expression, we nominate six bubbles identified from Simpson et al. (2012) catalogue by B1–B6. In Figure 5, all the bubbles are distributed along the CFG028.68–0.28 filament. The N49 infrared bubble is a very well-studied star forming region that consists of H II region G28.823–0.226 (e.g., Watson et al. 2008; Zavagno et al. 2010; Dewangan et al. 2017). The radio recombination line velocity toward the H II region was $\sim$ 90.6 km s^{-1} (Anderson & Bania 2009), which is just located between 83.5 and 95.5 km s^{-1} for the CO emission of CFG028.68–0.28. The H II region ionized by an O-type star is at a distance of 5.07 kpc (Dirienzo et al. 2012), which is associated with that of CFG028.68–0.28 (5.4 kpc). In addition, from Figure 6(a), we see that the ^{13}CO $J = 1-0$ emission adjacent to N49 shows arc-like structure with a very intense emission towards the filament, suggesting N49 is interacting with the CFG028.68–0.28 filament. Using the APEX 870 μm dust continuum data, Deharveng et al. (2010) reported the detection of at least four massive clumps toward the infrared rim of the bubble N49. The massive clumps are created by the expansion of N49. Figure 6(b) shows the ^{13}CO $J = 1-0$ emission map (blue contours) superimposed on temperature map (grey scale) derived from Hi-GAL survey data of CFG028.68–0.28. Compared with Figure 6(a), the regions with higher temperature are associated with the bubbles, while the regions with lower temperature are coincident with the infrared dark cloud. To clearly show the shape of these bubbles, we made the enlarged maps (Figs. 7 and 8). In Figure 7, N49 shows a bubble-like structure that is opened to southeast, indicating that the ionized gas has leaked from N49, whose direction is marked by two black arrows. In Figure 8, only three bubbles (B2, B3, and B6) show the ionized gas emission traced by the VLA 20 cm (red contours). Apart from B4, each bubble is associated with one or two *Herschel* 250 μm clumps. In particular, there is a clump located between B2 and B3.

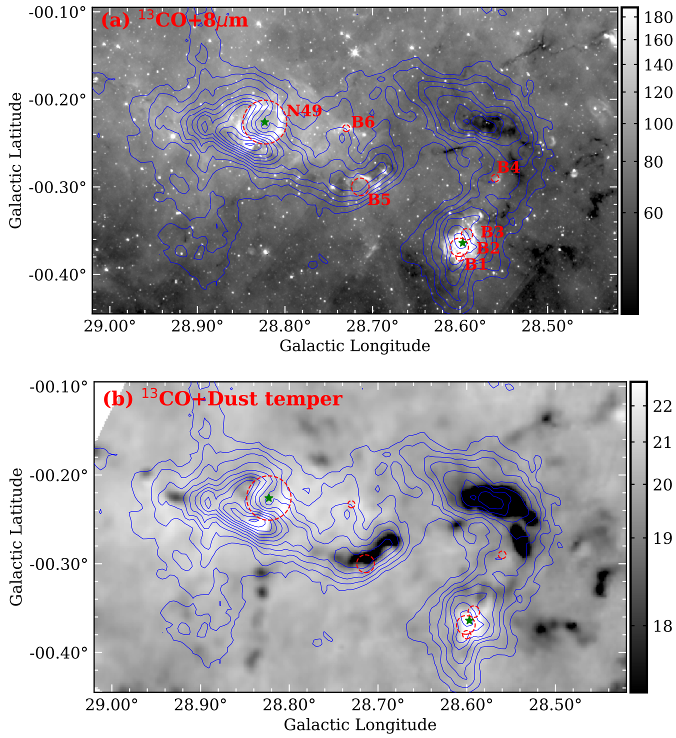

Fig. 6 (a) ^{13}CO $J = 1 - 0$ emission map (*blue contours*) superimposed on the *Spitzer*-IRAC 8 μm emission map (*grey scale*). The right colour bar is in units of MJy sr^{-1}. (b) ^{13}CO $J = 1 - 0$ emission map (*blue contours*) superimposed on dust temperature map (*grey scale*) derived from Hi-GAL survey data. The right color bar is the units of K. Both contour levels are from 5.0 (3σ) to 25.0 by a step of 2.5 K km s^{-1}. The red dashed circles represent infrared bubbles, while the green stars indicate H II regions.

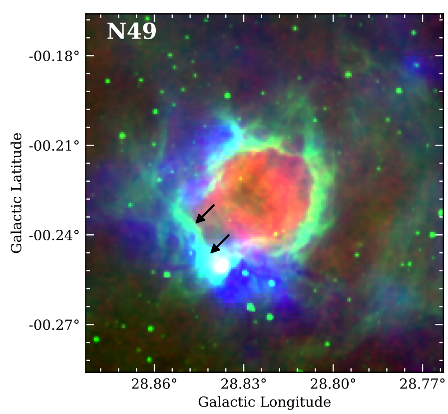

Fig. 7 Three-colour composite image of N49 using *Herschel* 250 μm (*blue*), *Spitzer*-IRAC 8 μm (*green*), and VLA 20 cm (*red*). The black arrows indicate the direction of the ionized gas leakage.

3.4 The Masses of the Selected Clumps in the Filament

Using the ATLASGAL catalog (Csengeri et al. 2014), we identified 27 dust clumps in the whole filament. These clumps are mainly distributed along the filament in Figure 9, while most of the clumps are located on the infrared dark part of the filament. We use the 870 μm flux of the clumps to estimate their masses. Assuming optically thin emission, the mass is given by (Hildebrand 1983)

$$M_{\rm clump} = \frac{S_\nu D^2}{\kappa_\nu B_\nu(T_d)} \tag{5}$$

where S_ν and D correspond to the flux density at the frequency ν and the distance to the clumps. The mass ratio of gas to dust was adopted as 100. κ_ν is the dust opacity, which is adopted as 0.01 cm^2 g^{-1} (Ossenkopf & Henning 1994) at 870 μm. $B_v(T_{\rm d})$ is the Planck function for the dust temperature T_d and frequency ν. The dust tempera-

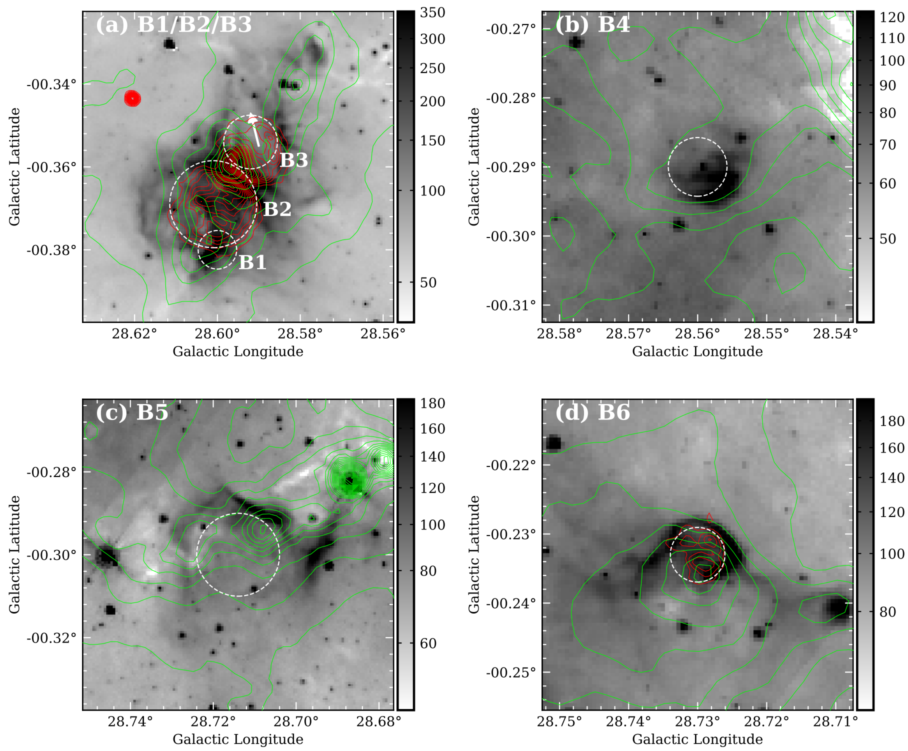

Fig. 8 In each panel, the *Herschel* 250 μm (*green contours*) and VLA 20 cm (*red contours*) emission overlaid on the *Spitzer*-IRAC 8 μm emission map (*grey scale*). The white dashed circles represent the identified bubbles. The right colour bar is units of MJy sr^{-1}. (a) The green contour levels begin from 5σ (1σ = 300 MJy sr^{-1}) in a step of 1σ, while the red contour levels begin from 3σ (1σ = 0.5 mJy beam^{-1}) in a step of 2σ. (b) The green contour levels begin from 5σ (1σ = 300 MJy sr^{-1}) in a step of 0.5σ. (c) The green contour levels begin from 5σ (1σ = 300 MJy sr^{-1}) in a step of 1σ. (d) The green contour levels begin from 5σ (1σ = 300 MJy sr^{-1}) in a step of 1σ, while the red contour levels begin from 3σ (1σ = 0.5 mJy beam^{-1}) in a step of 0.5σ.

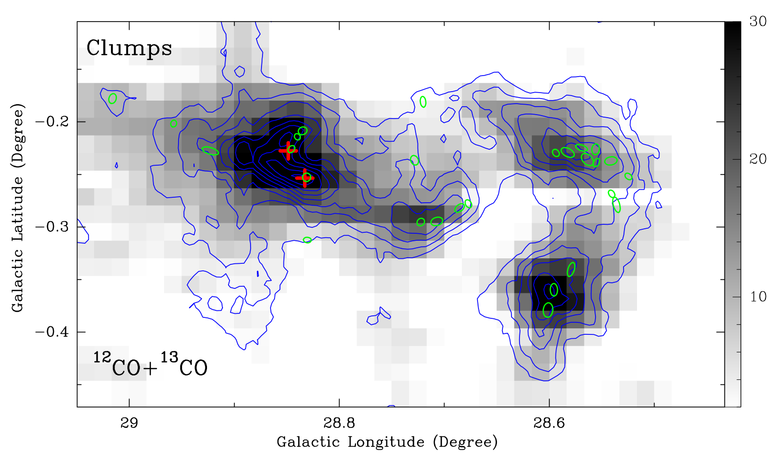

Fig. 9 Contours of ^{13}CO $J = 1 - 0$ emission superimposed on the ^{12}CO $J = 3 - 2$ emission (grey). Both integrated velocities are from 83.5 to 95.5 km s^{-1}. The blue contour levels are from 5.0 (3σ) to 25.0 by a step of 2.5 K km s^{-1}. The green ellipses represent the selected clumps. The two red pluses mark the EGO sources (Cyganowski et al. 2008). The right colour bar is given in units of K km s^{-1}.

tures of clumps are derived from the SEDs fit pixel by pixel through the Hi-GAL survey data.

Assuming that the clumps have roughly spherical shapes, the average volume density of each clump was calculated as

$$n_{\mathrm{H}_2} = \frac{M_{\mathrm{clump}}}{4/3\pi R_{\mathrm{eff}}^3 \mu m_{\mathrm{H}}}, \quad (6)$$

where $R_{\rm eff}$ is the effective radius of each clump, which is determined by

$$R_{\rm eff} = D\sqrt{\rm FWHM/2}, \tag{7}$$

where FWHM is the deconvolved size of the clumps. The obtained $R_{\rm eff}$ are listed in column 11 of Table 3.4. Clump radius ranges from 0.09 pc to 0.18 pc. The masses of these clumps range from 14 to 407 $M_\odot$ with a total mass of 1824 $M_\odot$, while the average volume density ranges from 3.1×10^4 to 3.8×10^5 cm^{-3}.

4 DISCUSSION

4.1 The Filament's Structure and Property

Previous 1.2 mm continuum observation with the IRAM 30 m single-dish telescope showed that IRDC G28.53–0.25 extends by about 5′ (Rathborne et al. 2006). Based on our ^{12}CO $J = 3-2$ and ^{13}CO $J = 1-0$ observations, CFG028.68–0.28 shows a filamentary structure extended by 40′ from east to west. From the column density ($N_{\rm H_2}$) map constructed from Hi-GAL survey data, we see that the column density map only shows four dense regions, not a continuous filamentary structure. We suggest that the previous identified IRDC G28.53–0.25 (5′) is only part of the larger filament CFG028.68–0.28. At 8 μm, IRDC G28.53–0.25 only displays a dark extinction feature about 5′ at the middle section of the filament. At each of the end sections of the filament, we find some bright Spitzer-IRAC 8 μm emission, which are associated with several infrared H II regions/bubbles. In addition, from the distribution of the dust temperature, we obtain that the regions with higher temperature in the filament are associated with the bubbles or H II regions, while the regions with lower temperature are coincident with the infrared dark cloud, suggesting that the ultraviolet (UV) radiation from the H II regions have ionized and heated the surrounding gas. The structure of the CFG028.68–0.28 filament is similar to that of the IRDC G34.43+0.24 filament, which also shows a 8 μm infrared dark and bright parts (Xu et al. 2016). The bright parts of the IRDC are associated with H II regions and infrared bubbles. The associated H II regions may have illuminated the dark parts of the filament making them bright, as in the description for an IRDC evolution given by Jackson et al. (2010). The effect of the ionizing radiation in the evolution of clouds and their star formation has been considered in numerical simulations (e.g., Dib et al. 2013; Kim et al. 2017). Hence, we suggest that H II regions that are created by massive stars play an important role in promoting the evolution of filamentary IRDC.

The formation of filaments is a natural consequence of turbulent cascades in the complex multiphase interstellar medium (Smith et al. 2016). If the turbulence is dominant, then a critical mass to length ratio can be estimated as $(M/l)_{\rm crit}$=84$(\Delta V)^2 M_\odot$ pc^{-1} (Chandrasekhar & Fermi 1953; Jackson et al. 2010), where $\triangle V$ is the full width at half-maximum (FWHM). Figure 10 shows the distribution of the FWHM for the ^{13}CO $J = 1-0$ emission in the filament. We found the mean FWHM of ^{13}CO $J = 1-0$ emission to be 3.0±0.4 km s^{-1}. Thus, we obtained $(M/l)_{\rm \ crit} \approx$ 756±202 $M_\odot$ pc^{-1}. Using the total mass ($(1.9\pm0.1)\times10^4 M_\odot$) and length (∼63 pc) of the filament, we obtained a linear mass density M/l of 305±16 $M_\odot$ pc^{-1}, which is smaller than $(M/l)_{\rm crit}$. Therefore, we conclude that external pressure from the neighboring bubbles and H II regions may help prevent the filament from dispersing under the effects of turbulence. We estimated the turbulent energy of the CFG028.68-0.28 filament using formula

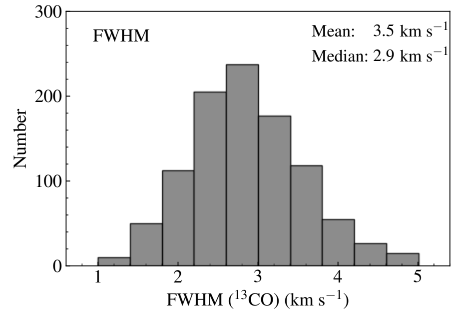

Fig. 10 Distribution of the full width at half-maximum (FWHM) for the filament. The number is all observed point whose emission is greater than 3 σ.

$$E_{\rm turb} = \frac{1}{2} M\sigma_{3d}^2, \tag{8}$$

where $\sigma_{3d} \approx \sqrt{3}\sigma_v$, which is the three-dimensional turbulent velocity dispersion. σ_v is $\triangle V/(2\sqrt{2\ln 2})$, and $\triangle V$ is the mean FWHM from the ^{13}CO $J = 1--0$ emission. In the filament, the mean thermal broadening can be given by $\Delta V_{\rm therm}$ =2.355×$\sqrt{kT_{\rm ex}/(\mu_g m({\rm H_2}))}$. Using an excitation temperature ($T_{\rm ex}$) of 4.4–18.0 K, we derived $\Delta V_{\rm therm}$ $\approx$ 0.3–0.5 km s^{-1}, which is much lower than the mean FWHM of 3.0 km s^{-1} measured for ^{13}CO J=1–0. Hence, we did not consider the velocity dispersion to be caused by thermal broadening. We obtained that the turbulent energy of the filament is about $(9.2 \pm 2.4)\times10^{47}$ erg. The turbulent dissipation rate of the filament can be calculated as $\dot{E}_{\rm turb} = E_{\rm turb}/t_{\rm diss}$, where $t_{\rm diss}$ is the turbulent dissipation time. According to McKee & Ostriker (2007), $t_{\rm diss} \sim d/2\sigma_v$, where d is the effective radius of the filament. We derived the turbulent dissipation time of 5.1 Myr, and the turbulent dissipation rate of $(7.8\pm2.0)\times10^{33}$ erg s^{-1} for the filament.

4.2 Clump Formation

Several cores and clumps in IRDC G28.53–0.25 are detected in high angular resolution observations (Rathborne

Table 1 Parameters of the Identified Dust Cores

ID	l (deg)	b (deg)	$\theta_{\rm maj}$ (arcsec)	$\theta_{\rm min}$ (arcsec)	PA (°)	FWHM (arcsec)	F_ν (Jy beam^{-1})	S_ν (Jy)	$T_{\rm dust}$ (K)	$R_{\rm eff}$ (pc)	$M_{\rm clump}$ ($M_\odot$)	$n_{\rm H_2}$ ($\times10^4$cm^{-3})
1	28.52	–0.25	27	19	141	23	0.52	0.73	16.9	0.10	25.9	8.8
2	28.54	–0.28	54	22	106	34	0.6	1.92	16.0	0.15	74.2	7.8
3	28.54	–0.27	28	19	124	23	0.47	0.66	15.8	0.10	26.0	8.8
4	28.54	–0.24	43	28	11	35	0.74	2.4	16.0	0.15	92.8	8.9
5	28.56	–0.24	31	19	58	24	0.42	0.69	15.3	0.10	28.7	8.6
6	28.56	–0.23	37	26	84	31	0.54	1.43	15.6	0.14	57.6	8.0
7	28.56	–0.24	50	32	134	40	1.97	8.45	14.0	0.17	407.3	26.3
8	28.57	–0.22	43	19	161	29	0.56	1.25	14.7	0.13	55.5	9.4
9	28.58	–0.34	50	22	72	33	0.68	2.06	19.8	0.14	57.4	6.6
10	28.58	–0.23	49	28	152	37	0.65	2.43	15.1	0.16	103.2	8.4
11	28.59	–0.23	27	21	129	24	0.43	0.65	16.0	0.10	25.1	7.5
12	28.60	–0.36	43	25	92	33	0.79	2.29	25.6	0.14	44.4	5.1
13	28.60	–0.38	50	33	83	41	0.51	2.29	23.0	0.18	51.4	3.1
14	28.68	–0.28	30	20	120	24	1.0	1.58	17.8	0.10	51.7	15.4
15	28.69	–0.28	38	23	38	30	1.04	2.46	19.2	0.13	71.7	11.0
16	28.71	–0.29	42	28	17	34	1.09	3.5	16.7	0.15	126.4	13.3
17	28.72	–0.18	37	19	97	27	0.41	0.78	19.8	0.12	21.7	4.6
18	28.72	–0.30	28	24	44	26	0.64	1.17	17.1	0.11	40.7	9.6
19	28.73	–0.24	34	26	115	30	0.42	1.0	21.7	0.13	24.4	3.7
20	28.83	–0.31	27	19	–5	23	0.4	0.57	18.1	0.10	18.2	6.2
21	28.83	–0.25	29	28	77	28	4.4	9.61	24.2	0.12	201.1	37.8
22	28.83	–0.21	31	26	25	29	0.86	1.92	20.5	0.13	50.8	8.6
23	28.84	–0.21	23	19	127	21	0.45	0.54	21.3	0.09	13.5	6.0
24	28.85	–0.23	28	20	47	24	0.51	0.78	20.3	0.10	20.9	6.3
25	28.92	–0.23	58	23	–17	37	0.59	2.14	18.5	0.16	66.0	5.4
26	28.96	–0.20	24	20	70	22	0.66	0.84	19.8	0.10	23.4	9.1
27	29.02	–0.18	35	25	72	30	0.61	1.47	19.0	0.13	43.5	6.7

The columns are as follows: (1) the source ID; (2)–(3) the positions in galactic coordinates; (4)–(5) the beam-convolved major and minor axes in arcseconds; (6) the position angle of the fitted Gaussian measured from north to east; (7) the average FWHM source size (beam-convolved); (8)–(9) the peak flux and the integrated flux.

et al. 2006, 2010; Sanhueza et al. 2012; Lu et al. 2015). Lu et al. (2015) suggested that some cores have star formation activities revealed by outflows, masers, or infrared sources. Using the ATLASGAL catalog, we identified 27 dust clumps in the CFG028.68–0.28 filament. The mass of the filament traced by ^{13}CO $J = 1 - 0$ emission is $\sim$1.9$\times10^4 M_\odot$, while the total mass of these selected dust clumps is 1824 $M_\odot$ in the filament. We can calculate a massive clump formation efficiency (CFE), which is given by $M_{\rm clump}/M_{\rm cloud}$. The obtained CFE in the CFG028.68–0.28 filament is $\sim$11%, which is consistent with the mean CFE (11%) in the GMC of the Milky Way (Battisti & Heyer 2014). Because the ATLASGAL catalogue listed the dense clump sample, the obtained CFE in the CFG028.68–0.28 filament is a lower limit. The presence of the infrared bubbles indicates that several massive stars have formed in the filament. To judge whether the selected dust clumps have sufficient mass to form massive stars, we consider their sizes and masses. According to Kauffmann & Pillai (2010), if the clump mass is $M(r) \geq 580 M_\odot (r/{\rm pc})^{1.33}$, then they can potentially form massive stars. Figure 11 presents a mass versus radius plot of the dust clumps embedded in the filament. From Figure 11, we obtained that 18 dust clumps lie at or above the threshold, indicating that

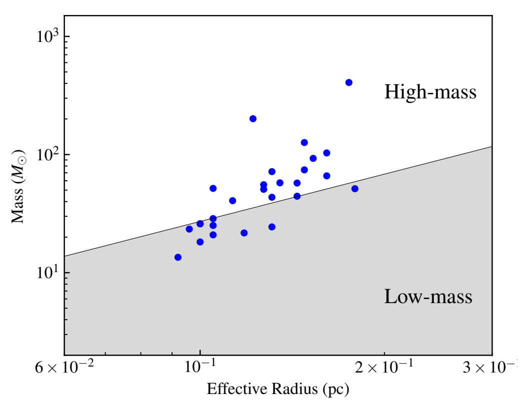

Fig. 11 Mass-Radius distribution for the ATLASGAL 870 μm clumps.

67% of these clumps are dense and massive enough to potentially form massive stars.

In a filament, the clump formation may be regulated by the interplay among gravity, turbulence, and magnetic field (Li et al. 2015). Turbulence in molecular clouds has been shown to dissipate quickly (Stone et al. 1998; Mac Low 1999), it needs to continuously drive turbulence via stellar feedback (Ostriker et al. 2010; Offner & Liu 2018). Massive stars are a possible mechanism for driving turbulence through feedback from outflows, UV radiation

Table 2 Physical and Calculated Parameters of Identified Infrared Bubbles

Name	l (deg)	b (deg)	Flux (mJy)	Age ($\times 10^6$ yr)	$E_{\rm k}$ ($\times 10^{47}$ erg)	$E_{\rm i}$ ($\times 10^{47}$ erg)	$E_{\rm t}$ ($\times 10^{47}$ erg)
N49	28.823	–0.256	–	0.5-1	1.9-3.6	32.8-54.7	2.1-3.5
MWP1G028600–003800S(B1)	28.600	–0.380	–	–	–	–	–
MWP1G028601–003690(B2)	28.601	–0.369	573(51)	0.6(0.1)	0.5(0.1)	7.9(1.1)	0.5(0.1)
MWP1G028592–003541(B3)	28.592	–0.354	386(34)	0.5(0.1)	0.3(0.1)	4.2(0.7)	0.3(0.1)
MWP1G028560–002900S(B4)	28.560	–0.290	–	–	–	–	–
MWP1G028714–003004(B5)	28.714	–0.300	–	–	–	–	–
MWP1G028730–002332(B6)	28.730	–0.230	31(7)	0.4(0.2)	0.1(0.1)	0.8(0.4)	0.1(0.1)

fields, stellar winds, and supernova explosions in molecular clouds. Extended green objects (EGOs) are considered as outflow candidate (Cyganowski et al. 2008). From the catalogue of Cyganowski et al. (2008), we found two EGO sources (G028.85–0.23 and G028.83–0.25) located in the CFG028.68–0.28 filament, as shown in Figure 9. Yang et al. (2018) have undertaken the largest survey for outflows within the Galactic plane using CO data for the ATLASGAL clumps. In the filamentary CFG028.68-0.28, we only found a clump with detected outflow, which is only associated with EGO G028.83–0.25 in space. The energy and dynamic time of the outflow are 4.0×10^{46} erg and 6.4×10^{4} yr, respectively. Moreover, Lu et al. (2015) found that other three cores are associated with outflows in IRDC G28.53–0.25 with high angular resolution observations. From Table 5 of Lu et al. (2015), we derived the total energy and mean dynamic time of the three outflows is 8.2×10^{46}erg and 6.4×10^{4} yr, respectively. Compared with the turbulent energy of the filamentary CFG028.68–0.28, all currently discovered outflows with a total energy of 1.2×10^{47} erg can not drive the observed turbulence in the filament.

H II regions and infrared bubbles were found to be associated with the CFG028.68–0.28 filament. Generally, infrared bubbles are created by the expansion of H II regions. We can calculate the kinetic energy, ionization energy, and thermal energy of these associated H II regions. According to Lasker (1967) and Freyer et al. (2003), the kinetic energy, ionization energy, and thermal energy can be estimated by

$$E_{\rm k} = \frac{4}{3}\pi n_i m_{\rm H} c_s^2 R_{\rm s}^{3/2}[(\frac{7}{4}c_s R_{\rm s}^{4/3} t_{\rm HII} + R_s^{7/4})^{6/7} - R_s^{3/2}], \tag{9}$$

$$E_{\rm i} = \frac{4}{3}\pi n_i(\frac{7}{4}c_s R_{\rm s}^{5/2} t_{\rm HII} + R_s^{7/2})^{6/7}\chi_0, \tag{10}$$

$$E_{\rm t} = \frac{4}{3}\pi n_i(\frac{7}{4}c_s R_{\rm s}^{5/2} t_{\rm HII} + R_s^{7/2})^{6/7} k T_{\rm II}, \tag{11}$$

where $m_{\rm H}$ is the mass of a hydrogen atom. $n_{\rm i}$ is the initial H number density of the molecular gas. $c_{\rm s}$ is the isothermal sound speed of ionized gas, assumed to be 10 km s^{-1}. $t_{\rm HII}$ represents the dynamical age of the H II region. χ_0 is the ionization potential of hydrogen in the ground state, and $T_{\rm II}$ is the effective electron temperature in the H II regions.

Assuming an H II region expanding in a homogeneous medium, the dynamical age $t_{\rm HII}$ was estimated via (Dyson & Williams 1980)

$$t_{\rm HII} = \frac{4R_{\rm s}}{7c_{\rm s}}[(\frac{R_{\rm HII}}{R_{\rm s}})^{7/4} - 1], \tag{12}$$

where $R_{\rm HII}$ is the radius of the H II region, and $R_{\rm s}$ is the radius of the Strömgren sphere given by $R_{\rm s} = (3N_{\rm Ly}/4\pi n_i^2 \alpha_B)^{1/3}$, where $N_{\rm Ly}$ is the ionizing luminosity, and $\alpha_B = 2.6\times10^{-13}$ cm^3 s^{-1} (Dyson & Williams 1980), which is the hydrogen recombination coefficient to all levels above the ground level. We used the volume-averaged H_2 (38.2 cm^{-3}) of the filament to determine $n_{\rm i}$ since the H II regions are located in the filament.

Using the 1.4 GHz radio continuum emission from the MAGPIS survey, the ionizing luminosity $N_{\rm Ly}$ was computed by Condon et al. (1998)

$$N_{\rm Ly} = 7.54\times10^{46}(\frac{\nu}{\rm GHz})^{0.1}(\frac{T_4}{\rm K})^{-0.45}(\frac{S_\nu}{\rm Jy})(\frac{D}{\rm kpc})^2\ {\rm s}^{-1}, \tag{13}$$

Where ν is the frequency of the observation, T_4 is the effective electron temperature in units of 10^4 K, S_ν is the observed specific flux density, and D is the distance to the H II region. Here we adopted an effective electron temperature of 10^4 K, and the distance (5.4 kpc) of the filament as those of the H II regions.

In our identified infrared bubbles, only N49, B2, B3, and B6 are associated with the 1.4 GHz radio continuum emission. N49 has been very well-studied. Using the APEX 870 μm dust continuum data, Deharveng et al. (2010) reported detection of at least four massive clumps toward the rim of the infrared bubble N49. The massive clumps are created by the expansion of N49. N49 shows a bubble-like structure that is opened at the southeast, suggesting that the ionized gas has leaked into the CFG028.68–0.28 filament. From Watson et al. (2008) and Zavagno et al. (2010), we directly adopt $R_{\rm s}$=2 pc and $t_{\rm HII}$=0.5–1 Myr for the H II region related to N49. From Figure 8, we measured a flux density at 1.4 GHz and a radius of ∼1.0 pc, 0.8 pc and ∼0.4 pc for the three H II regions associated with B2, B3, and B6, respectively. The obtained parameters are listed in Table 2. In Table 2, we obtained that the dynamical ages of the four H II regions associated with these bubbles, are one order of magnitude larger than that of the identified outflows. We infer that the ionizing stars of these infrared bubbles may be the first generation of stars that formed in CFG028.68–0.28. The driving sources of the outflows is likely to be the second generation of stars. The obtained total kinetic energy and thermal energy for the four H II regions are smaller than the turbulent energy (1.6×10^{48} erg) of filament CFG028.68–0.28. Compared to the kinetic energy and thermal energy, as well as the outflow energy, the ionization energy may inject more energy to CFG028.68–0.28, and help to drive the observed turbulence.

5 CONCLUSIONS

We present the ^{12}CO $J = 3-2$, ^{13}CO $J = 1-0$, ^{13}CO $J = 3-2$, infrared, and radio continuum observations toward CFG028.68–0.28 on a large scale. Based on the CO observations, CFG028.68–0.28 shows a quasi-sinusoidal filamentary structure extended by $40'$. Using the total mass of $\sim$1.8$\times$10$^4 M_\odot$ and length of $\sim$63 pc for the filament, we have obtained a linear mass density M/l of $\sim$ 305 $M_\odot$ pc^{-1}, which is smaller than $(M/l)_{\rm crit}$. This indicates that external pressure from the neighboring bubbles and H II regions may help to prevent the filament from dispersing under the effects of turbulence. From the ATLASGAL catalog, we identified 27 dust clumps in the whole CFG028.68–0.28 filament. About 67% of these clumps are dense enough and massive enough to potentially form massive stars. The obtained CFE is $\sim$ 11% in the CFG028.68–0.28 filament. Several infrared H II /bubbles at each end sections of the filament, suggest that the H II regions may play an important role in promoting the evolution of the CFG028.68–0.28 filament. We infer that the ionizing stars of these infrared bubbles may be the first generation of stars that formed in CFG028.68–0.28. Compared to the kinetic energy and thermal energy, as well as the outflow energy, the ionization energy may inject more energy to CFG028.68–0.28, and help drive the observed turbulence.

Acknowledgements We are very grateful to the referee for a timely report and helpful comments and suggestions that have improved the clarity of this paper. Thanks Nimei Chen, Yan Liu, Shao-Lin Long for their hard works during the CCOSMA telescope commissioning stage. Here we also thanks Li-Ping He, Dong-liang Liu, Jian-Ling Li, Jin-Quan Lv, Jin-Hua He, Tie Liu, Jian-Feng Zhou, Jarken Esimbek, Yang Gao, and so on for helps for the relocation and installation of the CCOSMA telescope. This work was supported by the National Natural Science Foundation of China (Grant Nos. 11363004, 11433008, 11633007, 11703040, 11743007, 11773014, 11847309 and 11851305), the Youth Innovation Promotion Association of CAS, the National Key R&D Programs of China (Nos. 2017YFA0402600 and 2015CB857100), and also supported by the Open Project Program of the Key Laboratory of FAST, NAOC, Chinese Academy of Sciences.

References

Anderson, L. D., & Bania, T. M. 2009, ApJ, 690, 706
André, P., Men'shchikov, A., Bontemps, S., et al. 2010, A&A, 518, L102
Battisti, A. J., & Heyer, M. H. 2014, ApJ, 780, 173
Benjamin, R. A., Churchwell, E., Babler, B. L., et al. 2003, PASP, 115, 953
Beuther, H., Linz, H., Tackenberg, J., et al. 2013, A&A, 553, A115
Beuther, H., Ragan, S. E., Johnston, K., et al. 2015, A&A, 584, A67
Carey, S. J., Feldman, P. A., Redman, R. O., et al. 2000, ApJ, 543, L157
Chandrasekhar, S., & Fermi, E. 1953, ApJ, 118, 116
Churchwell, E., Povich, M. S., Allen, D., et al. 2006, ApJ, 649, 759
Colombo, D., Rosolowsky, E., Duarte-Cabral, A., et al. 2019, MNRAS, 483, 4291
Condon, J. J., Cotton, W. D., Greisen, E. W., et al. 1998, AJ, 115, 1693
Contreras, Y., Garay, G., Rathborne, J. M., & Sanhueza, P. 2016, MNRAS, 456, 2041
Csengeri, T., Urquhart, J. S., Schuller, F., et al. 2014, A&A, 565, A75
Cyganowski, C. J., Whitney, B. A., Holden, E., et al. 2008, AJ, 136, 2391
Deharveng, L., Schuller, F., Anderson, L. D., et al. 2010, A&A, 523, A6
Dempsey, J. T., Thomas, H. S., & Currie, M. J. 2013, ApJS, 209, 8
Dewangan, L. K., Ojha, D. K., & Zinchenko, I. 2017, ApJ, 851, 140
Dib, S., Gutkin, J., Brandner, W., & Basu, S. 2013, MNRAS, 436, 3727
Dirienzo, W. J., Indebetouw, R., Brogan, C., et al. 2012, AJ, 144, 173
Dyson, J. E., & Williams, D. A. 1980, Physics of the interstellar medium (New York: Halsted Press)
Egan, M. P., Shipman, R. F., Price, S. D., et al. 1998, ApJ, 494, L199
Elmegreen, B. G. 2000, ApJ, 530, 277
Frerking, M. A., Langer, W. D., & Wilson, R. W. 1982a, ApJ, 262, 590
Frerking, M. A., Langer, W. D., & Wilson, R. W. 1982b, ApJ, 262, 590

Freyer, T., Hensler, G., & Yorke, H. W. 2003, ApJ, 594, 888
Garden, R. P., Hayashi, M., Gatley, I., Hasegawa, T., & Kaifu, N. 1991, ApJ, 374, 540
Griffin, M. J., Abergel, A., Abreu, A., et al. 2010, A&A, 518, L3
Helfand, D. J., Becker, R. H., White, R. L., Fallon, A., & Tuttle, S. 2006, AJ, 131, 2525
Hennebelle, P., Pérault, M., Teyssier, D., & Ganesh, S. 2001, A&A, 365, 598
Hildebrand, R. H. 1983, QJRAS, 24, 267
Jackson, J. M., Rathborne, J. M., Shah, R. Y., et al. 2006, ApJS, 163, 145
Jackson, J. M., Finn, S. C., Chambers, E. T., Rathborne, J. M., & Simon, R. 2010, ApJ, 719, L185
Kainulainen, J., Stutz, A. M., Stanke, T., et al. 2017, A&A, 600, A141
Kauffmann, J., & Pillai, T. 2010, ApJ, 723, L7
Kim, J.-G., Kim, W.-T., Ostriker, E. C., & Skinner, M. A. 2017, ApJ, 851, 93
Krumholz, M. R., Bate, M. R., Arce, H. G., et al. 2014, in Protostars and Planets VI, ed. H. Beuther, R. S. Klessen, C. P. Dullemond, & T. Henning, 243
Lasker, B. M. 1967, ApJ, 149, 23
Leger, A., & Puget, J. L. 1984, A&A, 137, L5
Li, G.-X., Urquhart, J. S., Leurini, S., et al. 2016, A&A, 591, A5
Li, H.-B., Yuen, K. H., Otto, F., et al. 2015, Nature, 520, 518
Lu, X., Zhang, Q., Wang, K., & Gu, Q. 2015, ApJ, 805, 171
Mac Low, M.-M. 1999, ApJ, 524, 169
McKee, C. F., & Ostriker, E. C. 2007, ARA&A, 45, 565
Molinari, S., Swinyard, B., Bally, J., et al. 2010, PASP, 122, 314
Offner, S. S. R., & Liu, Y. 2018, Nature Astronomy, 2, 896
Ossenkopf, V., & Henning, T. 1994, A&A, 291, 943
Ostriker, J. P., Choi, E., Ciotti, L., Novak, G. S., & Proga, D. 2010, ApJ, 722, 642
Palmeirim, P., André, P., Kirk, J., et al. 2013, A&A, 550, A38
Peretto, N., & Fuller, G. A. 2009, A&A, 505, 405
Poglitsch, A., Waelkens, C., Geis, N., et al. 2010, A&A, 518, L2
Rathborne, J. M., Jackson, J. M., Chambers, E. T., et al. 2010, ApJ, 715, 310
Rathborne, J. M., Jackson, J. M., & Simon, R. 2006, ApJ, 641, 389
Rigby, A. J., Moore, T. J. T., Plume, R., et al. 2016, MNRAS, 456, 2885
Robertson, B., & Goldreich, P. 2012, ApJ, 750, L31
Sanhueza, P., Jackson, J. M., Foster, J. B., et al. 2012, ApJ, 756, 60
Schneider, S., & Elmegreen, B. G. 1979, ApJS, 41, 87
Seifried, D., & Walch, S. 2015, MNRAS, 452, 2410
Simon, R., Rathborne, J. M., Shah, R. Y., Jackson, J. M., & Chambers, E. T. 2006, ApJ, 653, 1325
Simpson, R. J., Povich, M. S., Kendrew, S., et al. 2012, MNRAS, 424, 2442
Skrutskie, M. F., Cutri, R. M., Stiening, R., et al. 2006, AJ, 131, 1163
Smith, R. J., Glover, S. C. O., Klessen, R. S., & Fuller, G. A. 2016, MNRAS, 455, 3640
Stone, J. M., Ostriker, E. C., & Gammie, C. F. 1998, ApJ, 508, L99
Tackenberg, J., Beuther, H., Plume, R., et al. 2013, A&A, 550, A116
Veena, V. S., Vig, S., Mookerjea, B., et al. 2018, ApJ, 852, 93
Wang, K., Testi, L., Ginsburg, A., et al. 2015, MNRAS, 450, 4043
Wang, K., Testi, L., Burkert, A., et al. 2016, ApJS, 226, 9
Watson, C., Povich, M. S., Churchwell, E. B., et al. 2008, ApJ, 681, 1341
Xu, J.-L., Li, D., Zhang, C.-P., et al. 2016, ApJ, 819, 117
Yang, A. Y., Thompson, M. A., Urquhart, J. S., & Tian, W. W. 2018, ApJS, 235, 3
Zavagno, A., Anderson, L. D., Russeil, D., et al. 2010, A&A, 518, L101